Coupled Fault-Tolerant Control of Primary Permanent-Magnet Linear Motor Traction Systems for Subway Applications

Wei Wang, *Senior Member, IEEE*, Zhixiang Lu, Yanan Feng, Weijie Tian, Wei Hua, *Senior Member, IEEE*, Zheng Wang, *Senior Member, IEEE*, and Ming Cheng, *Fellow, IEEE*

***Abstract*—In this article, a coupled fault-tolerant control (C-FTC) is proposed for primary permanent-magnet linear motor traction system in subway applications. By coupling the faulty mover with a healthy mover, the proposed C-FTC can achieve continuous operation of the faulty mover, in which one or more current sensors fail. A healthy mover is determined as the reference mover. The switch-states of the reference mover are also applied to its mathematical model. As a result, synchronous currents of the reference mover are also estimated from its mathematical model, and they are treated as the reference currents of the mathematical model of the faulty mover. Hence, the switch-states of the faulty mover can be determined. Therefore, the faulty mover can be controlled without any current sensors. The key of C-FTC is to compensate the parameter variations and the nonlinear effects of the faulty mover drive system with those of a healthy mover drive system, which is the main contribution of this article. Comparing with the conventional current-sensorless control, C-FTC has stronger robustness to the parameter variations and the nonlinear effects. The effectiveness and robustness of the proposed C-FTC are verified by simulation and experimental results.**

***Index Terms*—Current-sensorless control (CSC), current reconstruction, fault-tolerance, primary permanent-magnet linear motor (PPMLM).**

I. Introduction

THE linear motor has received more and more attentions in subway applications [1]–[5]. It has several outstanding advantages are as follows:

1) direct production of the thrust force, which does not depend on the friction between wheel and rail;
2) smaller turning radius and smaller cross-sectional area, if a tunnel is required;
3) larger acceleration and stronger climbing ability;
4) lower noise and less maintenance.

Manuscript received February 29, 2020; revised July 2, 2020; accepted August 5, 2020. Date of publication August 11, 2020; date of current version October 30, 2020. This work was supported in part by the National Natural Science Foundation of China under Grants 51977036, 51991384, and 51607038, and in part by the ZhiShan Young Scholar Plan of Southeast University of China. Recommended for publication by Associate Editor J. Hur. *(Corresponding author: Wei Wang.)*

The authors are with the School of Electrical Engineering, Southeast University, Nanjing 210096, China (e-mail: wangwei1986@seu.edu.cn; luzhi401@foxmail.com; yanan_feng@foxmail.com; tianweijie@seu.edu.cn; huawei1978@seu.edu.cn; zwang@seu.edu.cn; mcheng@seu.edu.cn).

Color versions of one or more of the figures in this article are available online at https://ieeexplore.ieee.org.

Digital Object Identifier 10.1109/TPEL.2020.3015519

The linear induction motor (LIM) has been found in practical subway projects [6], [7]. However, the permanent-magnet linear motor (PMLM) s still not found in subway applications even though it has advantages of high efficiency and high power density [8], [9]. The main challenge faced by the conventional PMLM is the high construction cost. As is known, the stator of the LIM consists of iron while that of the conventional PMLM consists of magnets or armature windings [10]. Recently, a primary PMLM (PPMLM) has attracted more and more attentions, in which both magnets and armature windings can be mounted in movers (cars) [11]–[13]. Obviously, the construction cost of the PPMLM is still higher than that of the LIM while the structure also becomes more complicated. However, the construction cost of the PPMLM can be significantly reduced comparing to that of the conventional PMLM, which makes the practical utilization of PMLM in subway applications more possible.

For high-performance motor controls, such as field-oriented control (FOC) and direct thrust force control, two phase current sensors are usually required if three phase windings are connected together. If one phase current sensor fails, the three-phase linear motor usually cannot continue to work. As a result, the thrust force of the corresponding linear motor will be lost. Sometimes, however, the remaining thrust force is not enough for the continuous operation even though a subway train consists of several traction motors [14]. Therefore, the fault-tolerant control coping with current sensor faults is important for PPMLM traction systems. Fault diagnosis is the pre-condition of the fault-tolerant control, and many fault diagnosis methods have been proposed to detect the current sensor faults [15], [16].

Nowadays, many efforts have been made to reduce current sensors of motor drives, which can be considered as the fault-tolerant control to deal with current sensor faults. Current-sensorless controls (CSCs) can be easily thought since phase currents of electrical motors can be estimated by mathematical models. So far, a lot of CSCs have been proposed for various motors, such as induction motors (IMs) [17], synchronous reluctance motors [18], PMSMs [19], and double fed induction generators [20], respectively. Although all phase current sensors can be eliminated by using CSCs, their dependence on accurate motor models weakens the robustness. If there is one surviving phase current sensor, the system robustness may be enhanced by replacing one estimated phase current with the sensed value. In [21], the actual d- and q-axis currents are estimated from

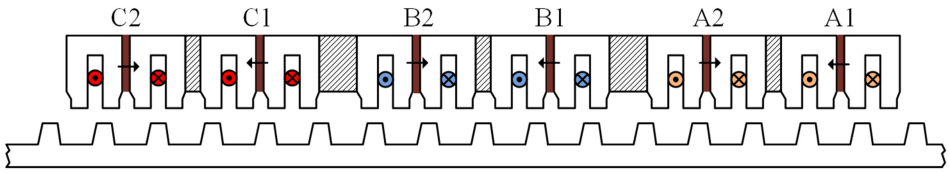

Fig. 1. Structure of the studied PPMLM.

the reference ones and the only surviving sensed phase current. During the estimation, no additional IM parameters are required. However, the transient performances are not satisfying [22]. In [23], a fault-tolerant control is proposed for IM drives against phase current sensor failures, in which the α- and β-axis currents are estimated by accurate IM model. The robustness of such fault-tolerant controls is improved by introducing a voltage decoupler module [24]. On the other hand, the dc-link current can reflect one phase current if the voltage-source-inverter (VSI) is operated with one active voltage vector. Furthermore, the reference voltage vector of pulsewidth modulation (PWM) based VSI is usually synthesized by two adjacent active voltage vectors, and they can reflect two different phase currents. Therefore, three phase currents can be reconstructed in one switching period by single dc-link current sensor for PWM-VSI if their summation is zero [20]. Obviously, the motor parameters are not required in the construction of phase currents. Unfortunately, this method is not suitable for the situation if the summation of all phase currents is not zero. So far, many control schemes using single dc-link current sensor have been presented [25]–[28]. However, sometimes the dc-link current sensor does not exist in motor drives.

All the abovementioned control methods only focus on single-motor drives while the subway traction system is a multimotor drive. This article proposes a coupled fault-tolerant control (C-FTC) for the PPMLM traction system, which takes full advantage of the multimotor feature. To clarify the description, the mover with one or more faulty current sensors is redefined as the faulty mover in this article. Furthermore, the conventional CSCs are renamed as independent fault tolerant controls (I-FTCs) since they only take the faulty mover into account. Differing from I-FTC, the faulty mover is coupled with one adjacent healthy mover in C-FTC. As is well-known, the performances of I-FTC will be seriously affected by the parameter variations and the nonlinear effects (dead-time and voltage drop of power devices) of the faulty mover drive system. By using C-FTC, however, these affections can be significantly reduced by compensating the parameter variations and the nonlinear effects of the faulty mover drive system with those of a healthy mover drive system, which is the main contribution of this article. The rest if article is organized as follows. The studied PPMLM traction system is defined in Section II. The proposed C-FTC is presented in Section III, and its performances are compared with I-FTC in Section IV. In order to verify the effectiveness of the C-FTC, some simulations and experiments are carried out in Sections V and VI, respectively. Finally, the conclusion is drawn in Section VII.

II. Studied PPMLM Traction System

A. System Topology

The structure of the studied PPMLM is shown in Fig. 1. Both magnets and armature windings are mounted in movers. The secondary is mounted in the rail. The topology of the studied PPMLM traction system is illustrated in Fig. 2, which contains four same three-phase movers (mover 1$\sim$mover 4). As shown in Fig. 2, four movers are, respectively, fed by four VSIs, and they are supplied by the contacting grid. The dc-link voltage u_{dc} is sensed by a voltage sensor. Obviously, independent control of four movers can be realized. For one mover, two phase currents are, respectively, sensed by two current sensors while the third phase current can be calculated. In this article, the phase windings of mover k ($k = 1\sim4$) are defined as phase-Ak, phase-Bk, and phase-Ck, respectively. The corresponding phase currents are defined as i_{ak}, i_{bk}, and i_{ck}, respectively. In this article, the subscript k represents Mover k.

B. Mathematical Model of PPMLM

The d- and q-axis of PPMLM are defined in Fig. 3. The d-axis is in the center of stator teeth, where the PM flux linkage is maximum. The q-axis is the primary position with the minimum (zero) PM flux linkage. The relative displacement between d- and q-axis is $\tau_s/4$, where τ_s is the stator pole pitch. When the positive PM flux linkage passing through phase-A winding is maximum, the corresponding primary position θ_e is defined as zero, as shown in Fig. 3.

Based on the definition earlier, the dynamic voltage equations of Mover k can be expressed as

$$\begin{cases} u_{dk} = R_s i_{dk} + \frac{d\psi_{dk}}{dt} - \omega\psi_{qk} \\ u_{qk} = R_s i_{qk} + \frac{d\psi_{qk}}{dt} + \omega\psi_{dk} \end{cases}, k = 1 \sim 4 \tag{1}$$

with

$$\begin{cases} \psi_{dk} = \psi_f + L_s i_{dk} \\ \psi_{qk} = L_s i_{qk} \end{cases} \tag{2}$$

$$\omega = 2\pi v_m/\tau_s \tag{3}$$

where ν_m is the mover speed; ψ_f is the PM flux linkage; i_{dk} and i_{qk} are d- and q-axis currents, respectively; u_{dk} and u_{qk} are d- and q-axis voltages, respectively; ψ_{dk} and ψ_{qk} are d- and q-axis stator flux linkages, respectively; and R_s and L_s are the stator resistance and inductance, respectively.

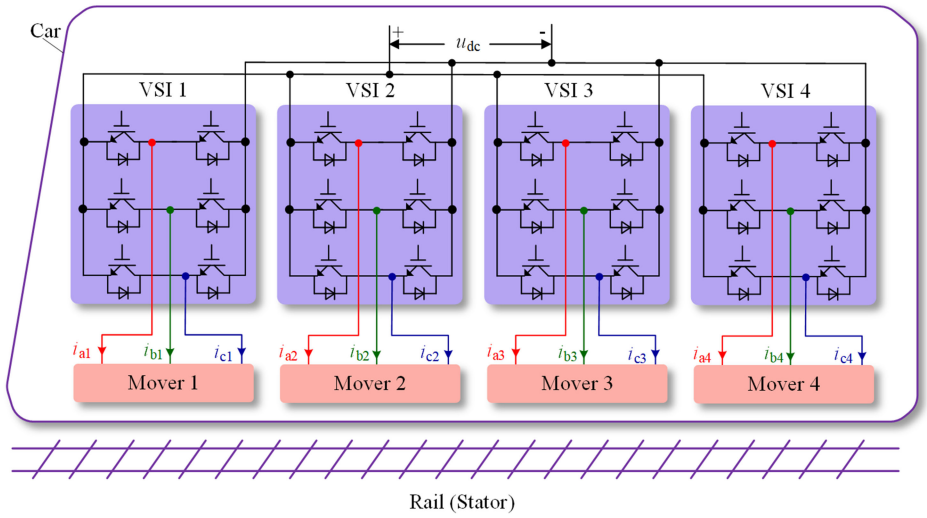

Fig. 2. Topology of the studied PPMLM traction system.

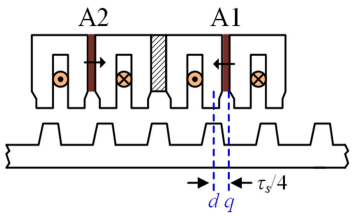

Fig. 3. Definition of d- and q-axis for PPMLM.

Substituting (2) into (1) gives

$$\begin{cases} u_{dk} = R_s i_{dk} + L_s \frac{di_{dk}}{dt} - \omega L_s i_{qk} \\ u_{qk} = R_s i_{qk} + L_s \frac{di_{qk}}{dt} + \omega(L_s i_{dk} + \psi_f) \end{cases}, k = 1 \sim 4. \tag{4}$$

In steady state, (4) can be simplified as

$$\begin{cases} u_{dk} = R_s i_{dk} - \omega L_s i_{qk} \\ u_{qk} = R_s i_{qk} + \omega(L_s i_{dk} + \psi_f) \end{cases}, k = 1 \sim 4. \tag{5}$$

Considering the linear motor mainly operates in transient states, (4) is more accurate than (5) since the transient-state operation is described by the differential terms in (4). However, the existence of the differential terms in (4) also will make the analysis difficult. In order to simplify the analysis, (5) is adopted in this article. According to (5), the electromagnetic thrust force is deduced as

$$F_{ek} = 3\pi\psi_f i_{qk}/\tau_s, k = 1 \sim 4. \tag{6}$$

III. Proposed C-FTC

Without special declaration, mover 2 is assumed to be the faulty mover while other movers are healthy, among which mover 1 is selected as the reference mover in this article. The selection principle of the reference mover will be explained in the following section. Therefore, phase currents of mover 1 can be sensed while one or more phase currents of mover 2 only can be estimated. To cope with all current sensor faults, all phase currents of mover 2 are estimated in this article. Based on this precondition, C-FTC is presented in this section, which is illustrated in Fig. 4. In this article, the superscripts $*$ and e represent the reference and estimated values, respectively. Additionally, the primary positions of two movers are measured by position sensors. C-FTC contains two modules: reference current generator and current sensorless controller, and they will be explained in the following content.

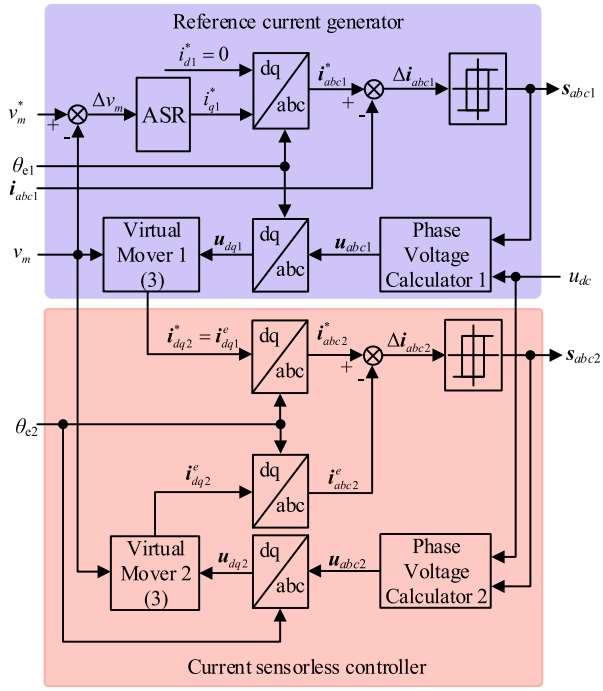

Fig. 4. Block diagram of the proposed C-FTC.

A. Reference Current Generator

In this module, the reference currents i^*_{dq2} of mover 2 are generated by the mathematical model of mover 1. The reference

q-axis current i_{q1}^* is determined by automatic speed regulator (ASR) while the reference d-axis current i_{d1}^* is set as 0. Then, the reference phase currents $\boldsymbol{i}_{abc1}^*$ can be obtained by the inverse Park transformation $\boldsymbol{Q}(\theta_{e1})$

$$\boldsymbol{i}_{abc1}^* = \boldsymbol{Q}(\theta_{e1})\boldsymbol{i}_{dq1}^* \tag{7}$$

with

$$\boldsymbol{Q}(\theta_{ek}) = \begin{bmatrix} \cos(\theta_{ek}) & -\sin(\theta_{ek}) \\ \cos(\theta_{ek}-2\pi/3) & -\sin(\theta_{ek}-2\pi/3) \\ \cos(\theta_{ek}+2\pi/3) & -\sin(\theta_{ek}+2\pi/3) \end{bmatrix}, k = 1, 2. \tag{8}$$

According to the hysteresis current control (HCC), the switch-states $\boldsymbol{s}_{abc1}$ of VSI 1 can be determined by comparing $\boldsymbol{i}_{abc1}^*$ with the actual phase currents $\boldsymbol{i}_{abc1}$. As a result, the synchronous currents $\boldsymbol{i}_{dq1}$ of Mover 1 can be well controlled.

Meanwhile, the estimated synchronous currents $\boldsymbol{i}_{dq1}^e$ are calculated by the mathematical model (4), which is defined as the virtual reference mover. According to (4), the synchronous voltages $\boldsymbol{u}_{dq1}$ are required. Based on the phase voltages $\boldsymbol{u}_{abc1}$ and the primary position θ_{e1}, $\boldsymbol{u}_{dq1}$ can be obtained by Park transformation $\boldsymbol{P}(\theta_{e1})$

$$\boldsymbol{u}_{dq1} = \boldsymbol{P}(\theta_{e1})\boldsymbol{u}_{abc1} \tag{9}$$

with

$$\boldsymbol{P}(\theta_{ek}) = (2/3) \begin{bmatrix} \cos(\theta_{ek}) & \cos(\theta_{ek}-2\pi/3) & \cos(\theta_{ek}+2\pi/3) \\ -\sin(\theta_{ek}) & -\sin(\theta_{ek}-2\pi/3) & -\sin(\theta_{ek}+2\pi/3) \\ 0.5 & 0.5 & 0.5 \end{bmatrix}, k = 1, 2. \tag{10}$$

The phase voltages $\boldsymbol{u}_{abc1}$ can be reconstructed from the switch-states $\boldsymbol{s}_{abc1}$ and the dc-link voltage u_{dc}

$$\begin{bmatrix} u_{a1} \\ u_{b1} \\ u_{c1} \end{bmatrix} = \frac{1}{3} u_{\mathrm{dc}} \begin{bmatrix} 2 & -1 & -1 \\ -1 & 2 & -1 \\ -1 & -1 & 2 \end{bmatrix} \begin{bmatrix} s_{a1} \\ s_{b1} \\ s_{c1} \end{bmatrix}. \tag{11}$$

Therefore, the estimated synchronous currents $\boldsymbol{i}_{dq1}^e$ can be obtained by the virtual reference mover.

It can be found that the synchronous voltages $\boldsymbol{u}_{dq1}$ are first determined by the actual mover 1 and then supplied on the virtual mover 1 to generate the estimated synchronous currents $\boldsymbol{i}_{dq1}^e$. It should be emphasized that $\boldsymbol{i}_{dq1}^e$ have no influences on the control of the actual mover 1.

In C-FTC, the estimated synchronous currents $\boldsymbol{i}_{dq1}^e$ of the virtual mover 1 are treated as the reference values $\boldsymbol{i}_{dq2}^*$ of the virtual mover 2, that is

$$\boldsymbol{i}_{dq2}^* = \boldsymbol{i}_{dq1}^e. \tag{12}$$

B. Current Sensorless Controller

In this module, mover 2 is controlled according to $\boldsymbol{i}_{dq2}^*$ without any current sensor. Based on the inverse Park transformation (8), the reference phase currents $\boldsymbol{i}_{abc2}^*$ can be obtained as follows:

$$\boldsymbol{i}_{abc2}^* = \boldsymbol{Q}(\theta_{e2})\boldsymbol{i}_{dq2}^*. \tag{13}$$

HCC is also selected for mover 2, which usually generates the switch-states $\boldsymbol{s}_{abc2}$ by comparing $\boldsymbol{i}_{abc2}^*$ with the actual phase currents $\boldsymbol{i}_{abc2}$. However, $\boldsymbol{i}_{abc2}$ can not be obtained since there are not enough healthy current sensors for mover 2, which is the trouble. Instead, $\boldsymbol{i}_{abc2}$ are replaced by the estimated phase currents $\boldsymbol{i}_{abc2}^e$.

According to Fig. 2, four movers share one common dc-link voltage u_{dc}, which can be sensed by the dc-link voltage sensor. When $\boldsymbol{s}_{abc2}$ are applied on VSI 2, the actual phase voltages $\boldsymbol{u}_{abc2}$ can be reconstructed as follows:

$$\begin{bmatrix} u_{a2} \\ u_{b2} \\ u_{c2} \end{bmatrix} = \frac{1}{3} u_{dc} \begin{bmatrix} 2 & -1 & -1 \\ -1 & 2 & -1 \\ -1 & -1 & 2 \end{bmatrix} \begin{bmatrix} s_{a2} \\ s_{b2} \\ s_{c2} \end{bmatrix}. \tag{14}$$

Hence, the synchronous voltages $\boldsymbol{u}_{dq2}$ can be calculated from the Park transformation (10)

$$\boldsymbol{u}_{dq2} = \boldsymbol{P}(\theta_{e2})\boldsymbol{u}_{abc2}. \tag{15}$$

According to $\boldsymbol{u}_{dq2}$ and the mover speed v_m, the estimated synchronous currents $\boldsymbol{i}_{dq2}^e$ are calculated from (4), and then the estimated phase currents $\boldsymbol{i}_{abc2}^e$ can be finally obtained from the inverse Park transformation

$$\boldsymbol{i}_{abc2}^e = \boldsymbol{Q}(\theta_{e2})\boldsymbol{i}_{dq2}^e. \tag{16}$$

The switch-states $\boldsymbol{s}_{abc2}$ determined by the virtual mover 2 are also applied to the actual mover 2. Finally, the actual mover 2 can be successfully controlled.

IV. Performance Analysis

The performances of the proposed C-FTC and the conventional I-FTC are analyzed in this section.

A. Affections of Parameter Variation for I-FTC

In this section, the nonlinear effects of VSIs are neglected. To clarify the analysis, the block diagram of I-FTC is deduced from Fig. 4, which is illustrated in Fig. 5. In I-FTC, the reference synchronous currents $\boldsymbol{i}_{dq2}^*$ of the faulty mover (mover 2) are directly set as the reference synchronous currents $\boldsymbol{i}_{dq1}^*$ of the healthy mover (mover 1), that is,

$$\begin{cases} i_{d2}^* = i_{d1}^* \\ i_{q2}^* = i_{q1}^*. \end{cases} \tag{17}$$

As a result, the synchronous currents of both movers are independent.

It is assumed that $\boldsymbol{i}_{dq2}^*$ can be well tracked by the estimated synchronous currents $\boldsymbol{i}_{dq2}^e$, that is,

$$\begin{cases} i_{d2}^e = i_{d2}^* \\ i_{q2}^e = i_{q2}^*. \end{cases} \tag{18}$$

Substituting (17) into (5) gives

$$\begin{cases} u_{d2} = R_s i_{d2}^* - \omega L_s i_{q2}^* \\ u_{q2} = R_s i_{q2}^* + \omega(L_s i_{d2}^* + \psi_f) \end{cases} \tag{19}$$

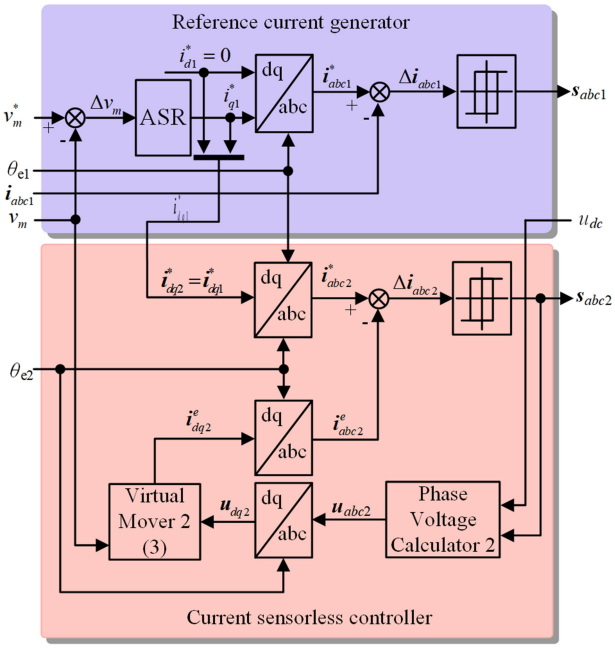

Fig. 5. Block diagram of the conventional I-FTC.

where ψ_f, R_s and L_s are redefined as the rated PM flux linkage, the rated stator resistance, and inductance, respectively. Considering the parameter variations and the actual synchronous currents $\boldsymbol{i}_{dq2}$ of mover 2, (5) also can be rewritten as

$$\begin{cases} u_{d2} = R_{s2} i_{d2} - \omega L_{s2} i_{q2} \\ u_{q2} = R_{s2} i_{q2} + \omega (L_{s2} i_{d2} + \psi_{f2}) \end{cases} \tag{20}$$

where ψ_{f2}, R_{s2}, and L_{s2} are the actual PM flux linkage, the actual stator resistance, and inductance of mover 2, respectively. The relationship between (ψ_f, R_s, L_s) and (ψ_{f2}, R_{s2}, L_{s2}) is defined as

$$\begin{cases} R_{s2} = \eta_{R2} R_s \\ L_{s2} = \eta_{L2} L_s \\ \psi_{f2} = \eta_{\psi 2} \psi_f \end{cases} \tag{21}$$

where $\eta_{\psi 2}$, η_{R2}, and η_{L2} are the variation coefficients of PM flux linkage, stator resistance, and inductance of mover 2, respectively. According to (17)–(21), the relationship of (i_{d1}^*,i_{q1}^*) and (i_{d2}, i_{q2}) can be determined by (22), as shown at the bottom of this page. According to (22), the actual synchronous currents $\boldsymbol{i}_{dq2}$ of mover 2 will be seriously affected by the parameter variations. In other words, the performances of I-FTC highly depend on the accuracy of mover parameters, which is the main drawback of I-FTC.

B. Affections of Parameter Variation for C-FTC

In this section, the nonlinear effects of VSIs are also neglected. The analysis in this section refers to Fig. 4. It is assumed that $\boldsymbol{i}_{dq1}^*$ can be well tracked by the actual synchronous currents $\boldsymbol{i}_{dq}$, that is,

$$\begin{cases} i_{d1} = i_{d1}^* \\ i_{q1} = i_{q1}^*. \end{cases} \tag{23}$$

Substituting (23) into (5) gives

$$\begin{cases} u_{d1} = R_{s1} i_{d1}^* - \omega L_{s1} i_{q1}^* \\ u_{q1} = R_{s1} i_{q1}^* + \omega (L_{s1} i_{d1}^* + \psi_{f1}). \end{cases} \tag{24}$$

Considering the parameter variations and the estimated synchronous currents $\boldsymbol{i}_{dq1}^e$ of mover 1, (5) also can be rewritten as

$$\begin{cases} u_{d1} = R_s i_{d1}^e - \omega L_s i_{q1}^e \\ u_{q1} = R_s i_{q1}^e + \omega (L_s i_{d1}^e + \psi_f) \end{cases} \tag{25}$$

where ψ_{f1}, R_{s1}, and L_{s1} are the actual PM flux linkage, the actual stator resistance, and inductance of Mover 1, respectively. The relationship between (ψ_f, R_s, L_s) and (ψ_{f1}, R_{s1}, L_{s1}) is defined as

$$\begin{cases} R_{s1} = \eta_{R1} R_s \\ L_{s1} = \eta_{L1} L_s \\ \psi_{f1} = \eta_{\psi 1} \psi_f \end{cases} \tag{26}$$

where $\eta_{\psi 1}$, η_{R1}, and η_{L1} are the variation coefficients of PM flux linkage, stator resistance, and inductance of mover 1, respectively.

In C-FTC, the reference synchronous currents $\boldsymbol{i}_{dq2}^*$ of mover 2 are indirectly set as the estimated synchronous currents $\boldsymbol{i}_{dq1}^e$, that is,

$$\begin{cases} i_{d2}^* = i_{d1}^e \\ i_{q2}^* = i_{q1}^e. \end{cases} \tag{27}$$

According to (27), $\boldsymbol{i}_{dq2}^*$ is the bridge between $\boldsymbol{i}_{dq1}^e$ and $\boldsymbol{i}_{dq2}^e$, and the virtual faulty mover and the healthy one are coupled together. According to (18), (19), (25), and (27), $\boldsymbol{u}_{dq1}$ should be equal to $\boldsymbol{u}_{dq2}$, that is,

$$\begin{cases} u_{d1} = u_{d2} \\ u_{q1} = u_{q2}. \end{cases} \tag{28}$$

$$\begin{cases} i_{d2} = \dfrac{[\eta_{R2}(R_s)^2 + \eta_{L2}(\omega L_s)^2] i_{d1}^* + (\eta_{L2} - \eta_{R2}) \omega R_s L_s i_{q1}^* + (1 - \eta_{\psi 2}) \eta_{L2} \omega^2 L_s \psi_f}{(\eta_{R2} R_s)^2 + (\eta_{L2} \omega L_s)^2} \\ i_{q2} = \dfrac{(\eta_{R2} - \eta_{L2}) \omega R_s L_s i_{d1}^* + [\eta_{R2}(R_s)^2 + \eta_{L2}(\omega L_s)^2] i_{q1}^* + (1 - \eta_{\psi 2}) \eta_{R2} \omega R_s \psi_f}{(\eta_{R2} R_s)^2 + (\eta_{L2} \omega L_s)^2} \end{cases} \tag{22}$$

$$\begin{cases} i_{d2} = \dfrac{[\eta_{R1}\eta_{R2}(R_s)^2 + \eta_{L1}\eta_{L2}(\omega L_s)^2] i_{d1}^* + (\eta_{L2}\eta_{R1} - \eta_{R2}\eta_{L1}) \omega R_s L_s i_{q1}^* + (\eta_{\psi 1} - \eta_{\psi 2}) \eta_{L2} \omega^2 L_s \psi_f}{(\eta_{R2} R_s)^2 + (\eta_{L2} \omega L_s)^2} \\ i_{q2} = \dfrac{(\eta_{R2}\eta_{L1} - \eta_{L2}\eta_{R1}) \omega R_s L_s i_{d1}^* + [\eta_{R1}\eta_{R2}(R_s)^2 + \eta_{L1}\eta_{L2}(\omega L_s)^2] i_{q1}^* + (\eta_{\psi 1} - \eta_{\psi 2}) \eta_{R2} \omega R_s \psi_f}{(\eta_{R2} R_s)^2 + (\eta_{L2} \omega L_s)^2} \end{cases} \tag{29}$$

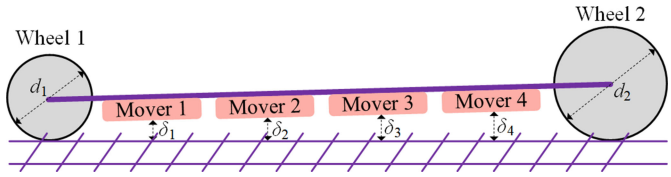

Fig. 6. Diagram of airgap width variation.

According to (20), (24), and (28), the relationship of (i_{d1}^*, i_{q1}^*) and (i_{d2}, i_{q2}) can be determined by (29) shown at the bottom of this page.

According to (29), the actual synchronous currents $\boldsymbol{i}_{dq2}$ of mover 2 are affected by the parameter variations of two movers in C-FTC instead of just mover 2 in I-FTC. It seems that C-FTC will perform worse than I-FTC. However, the fact is not like this in subway applications. As is mentioned in the Section II-A, all movers are required to have same rated parameters in a subway train. Due to the machining error, however, the actual parameters may be different between any two movers but these differences should be quite small. Otherwise, the mover is not qualified. Additionally, the actual mover parameters also can be affected by the operation conditions, such as flux saturation and temperature. In order to minimize the parameter differences between the faulty mover and the reference one, the reference mover is determined according the nearest selection principle, which will be explained in the Section IV-C. Hence, the reference mover and the faulty one have nearly same operation conditions. As a result, the parameter variations of two movers should be nearly same, that is

$$\begin{cases} \eta_{R1} \approx \eta_{R2} \\ \eta_{L1} \approx \eta_{L2} \\ \eta_{\psi 1} \approx \eta_{\psi 2}. \end{cases} \tag{30}$$

Substituting (30) into (29) gives

$$\begin{cases} i_{d2} \approx i_{d1}^* \\ i_{q2} \approx i_{q1}^*. \end{cases} \tag{31}$$

According to (31), the actual synchronous currents $\boldsymbol{i}_{dq2}$ of mover 2 can well track the reference values $\boldsymbol{i}_{dq1}^*$ of mover 1 by using C-FTC. Comparing with I-FTC, C-FTC has stronger robustness to parameter variations.

C. Nearest Selection Principle

As is analyzed in Section IV-B, the parameter variations are mainly resulted by the different operation conditions of the faulty and the reference movers. Hence, a selection principle is proposed in this section to choose a preferable healthy mover as the reference mover.

Due to the friction dissipation and the machining error, the wheel diameter difference usually cannot be avoided, as illustrated in Fig. 6. Therefore, the airgap widths of all movers become different. Obviously, the airgap width difference between two adjacent movers is minimum. On the other hand, the permanent-magnet flux linkage and the mover inductance highly depend on the airgap width. In order to minimize the parameter differences between the faulty and reference movers, the healthy mover nearest to the faulty mover should be selected as the reference mover for the proposed C-FTC. Therefore, this selection principle is named as the nearest selection principle. As a multimover drive, the candidate of the reference mover usually is not unique. For example, both mover 1 and 3 can be selected as the reference mover if mover 2 fails according to Fig. 2.

According to [14], the available maximum diameter difference is 10 mm, which is too small comparing to the length of one subway car. Therefore, the diameter difference can be ignored.

D. Nonlinear Effects of VSIs

In this section, the parameter variation are neglected, and the nonlinear effects of VSIs will be evaluated for C-FTC and I-FTC. Hence, (24), (25), (19), and (20) can be, respectively, rewritten as

$$\begin{cases} u_{d1} + \Delta u_{d1} = R_s i_{d1}^* - \omega L_s i_{q1}^* \\ u_{q1} + \Delta u_{q1} = R_s i_{q1}^* + \omega (L_s i_{d1}^* + \psi_f) \end{cases} \tag{32}$$

$$\begin{cases} u_{d1} = R_s i_{d1}^e - \omega L_s i_{q1}^e \\ u_{q1} = R_s i_{q1}^e + \omega (L_s i_{d1}^e + \psi_f) \end{cases} \tag{33}$$

$$\begin{cases} u_{d2} = R_s i_{d2}^* - \omega L_s i_{q2}^* \\ u_{q2} = R_s i_{q2}^* + \omega (L_s i_{d2}^* + \psi_f) \end{cases} \tag{34}$$

$$\begin{cases} u_{d2} + \Delta u_{d2} = R_s i_{d2} - \omega L_s i_{q2} \\ u_{q2} + \Delta u_{q2} = R_s i_{q2} + \omega (L_s i_{d2} + \psi_f) \end{cases} \tag{35}$$

where Δu_{d1} and Δu_{q1} are the d- and q-axis voltage errors caused by the nonlinear effects of VSI 1, respectively; and Δu_{d2} and Δu_{q2} are the d- and q-axis voltage errors caused by the nonlinear effects of VSI 2, respectively.

For I-FTC, the relationship of (i_{d1}^*, i_{q1}^*) and (i_{d2}, i_{q2}) can be determined from (17), (34), and (35) as

$$\begin{cases} i_{d2} = i_{d1}^* + \frac{R_s \Delta u_{d2} + \omega L_s \Delta u_{q2}}{R_s^2 + (\omega L_s)^2} \\ i_{q2} = i_{q1}^* + \frac{R_s \Delta u_{q2} - \omega L_s \Delta u_{d2}}{R_s^2 + (\omega L_s)^2}. \end{cases} \tag{36}$$

According to (36), the static errors between (i_{d1}^*, i_{q1}^*) and (i_{d2}, i_{q2}) will appear. Hence, the performances of I-FTC will be affected by the nonlinear effects of VSI 2.

For C-FTC, the relationship of (i_{d1}^*, i_{q1}^*) and (i_{d2}, i_{q2}) can be determined from (17), (28), (32), and (35) as

$$\begin{cases} i_{d2} = i_{d1}^* - \frac{(\Delta u_{d1} - \Delta u_{d2}) R_s + (\Delta u_{q1} - \Delta u_{q2}) \omega L_s}{R_s^2 + (\omega L_s)^2} \\ i_{q2} = i_{q1}^* - \frac{(\Delta u_{q1} - \Delta u_{q2}) R_s - (\Delta u_{d1} - \Delta u_{d2}) \omega L_s}{R_s^2 + (\omega L_s)^2}. \end{cases} \tag{37}$$

According to (37), it seems that the performances of C-FTC will be affected by the nonlinear effects of VSI 1 and VSI 2 at the same time. Due to the nearly same operation conditions, the nonlinear effects of two VSIs can be considered to be same, that is,

$$\begin{cases} \Delta u_{d1} = \Delta u_{d2} \\ \Delta u_{q1} = \Delta u_{q2}. \end{cases} \tag{38}$$

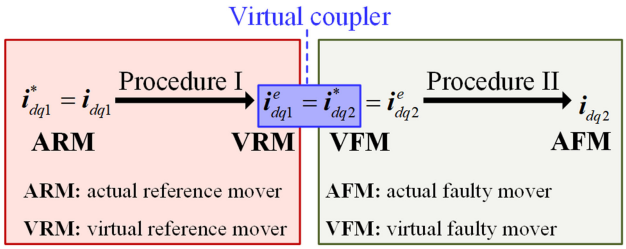

Fig. 7. Two procedures of C-FTC.

As a result, no static errors between (i_{d1}^*, i_{q1}^*) and (i_{d2}, i_{q2}) will appear in ideal situation. Even though the nonlinear effects of two VSIs may be a bit different in actual situation, C-FTC performs better robustness to the nonlinear effects of VSIs.

E. Discussion

In C-FTC, there are two procedures, which are illustrated in Fig. 7. In procedure I, the signal flow is from the actual reference mover to the virtual reference mover, and the parameter variations and the nonlinear effects are neglected. In procedure II, the signal flow is from the virtual faulty mover to the actual faulty mover, and the parameter variations and the nonlinear effects are added. It can be found that they are two reversible procedures. Without (27), these two procedures are independent. However, they are coupled together due to the introduction of the virtual coupler (27). The affections of the parameter variations and the nonlinear effects during procedure II can be automatically compensated by procedure I, which is the main contribution of this article. However, it is not necessary to know the exact values of the parameter variations and the nonlinear effects. In order to minimize the differences of actual parameters between any two movers, all movers should have nearly same rated parameters and they also should have nearly same operation conditions. These requirements can be easily realized for subway trains. First, the parameter consistency is a basic requirement for mature commercial productions. Therefore, the differences of rated parameters between any two movers in a subway train can be quite small. Second, the reference mover is selected from the adjacent movers of the faulty mover. Therefore, the differences of operation conditions between two movers in a subway train also can be quite small. Therefore, the affections of parameter variations and the nonlinear effects can be nearly same for both the reference and faulty movers. Therefore, the performances of C-FTC are nearly not affected by the parameter variations and the nonlinear effects. No matter how much the differences of actual parameters between two movers, to say the least, the performances of C-FTC should be better than those of I-FTC.

F. Applications

In real subway applications, the current sensor faults can be detected by existing fault diagnosis methods [15], [16]. Once one or more current sensors are detected to be failed, the corresponding mover is set as the faulty mover immediately. Then, the reference mover is determined according to the nearest selection principle. Third, the reference synchronous currents of the faulty mover are switched from ASR to the virtual reference mover, and C-FTC is activated. Finally, the actual currents of the faulty mover can be virtually measured by the reference mover using C-FTC.

TABLE I
PARAMETERS OF PPMLM

Parameter	Value
Mover resistance (Ω), R_s	3
Mover inductance (mH), L_s	33.5
Permanent-magnet flux linkage (Wb), ψ_f	0.125
Rate phase current (A)	3
Rated speed (m/s)	1.2
Maximum load (N)	150

TABLE II
DEFINITION OF FOUR SITUATIONS FOR CONTROLLERS

Situation	Mover resistance	Mover inductance	Permanent-magnet flux linkage
Situation-1	R_s	L_s	ψ_f
Situation-2	$2R_s$	L_s	ψ_f
Situation-3	R_s	L_s	$0.5\psi_f$
Situation-4	R_s	$0.5L_s$	ψ_f

V. SIMULATION VALIDATION

In order to verify the effectiveness of the proposed C-FTC, a MATLAB/Simulink model is developed, and some simulation results are provided. The parameters of PPMLM are given in Table I. The dc-link voltage is 50 V. The sampling frequency is 20 kHz. The reference speed is set as 0.3 m/s. Several simulations are carried out to verify the effectiveness of C-FTC.

A. Simulation 1: Affections of Same Parameter Variations

In this simulation, actual parameters of all movers are equal to the rated values (see Table I) while the controller parameters are given in Table II. In other words, both movers have same parameter variations. Additionally, the nonlinear effects are neglected. The simulation results using C-FTC are illustrated in Fig. 8. As shown in Fig. 8, the estimated synchronous currents are significantly affected by parameter variations, and they are varied in four situations. However, the estimated synchronous currents of mover 1 can be well tracked by those of mover 2 no matter in which situation, and the actual synchronous currents in four situations are not affected by the parameter variations. Especially, both movers always can output same synchronous currents no matter in which situations. Hence, the performances of C-FTC are not affected if both movers have same parameter variations.

B. Simulation 2: Affections of Different Parameter Variations

In this simulation, the actual resistance, inductance, and permanent-magnet flux linkage of mover 2 are set as $0.9R_s$, $0.9L_s$, and $1.1\psi_f$, respectively. Situation-3 and situation-4 are selected as two examples to verify the theoretical analysis. Other simulation parameters in this simulation are as same as those in simulation 1. Hence, both movers have different parameter

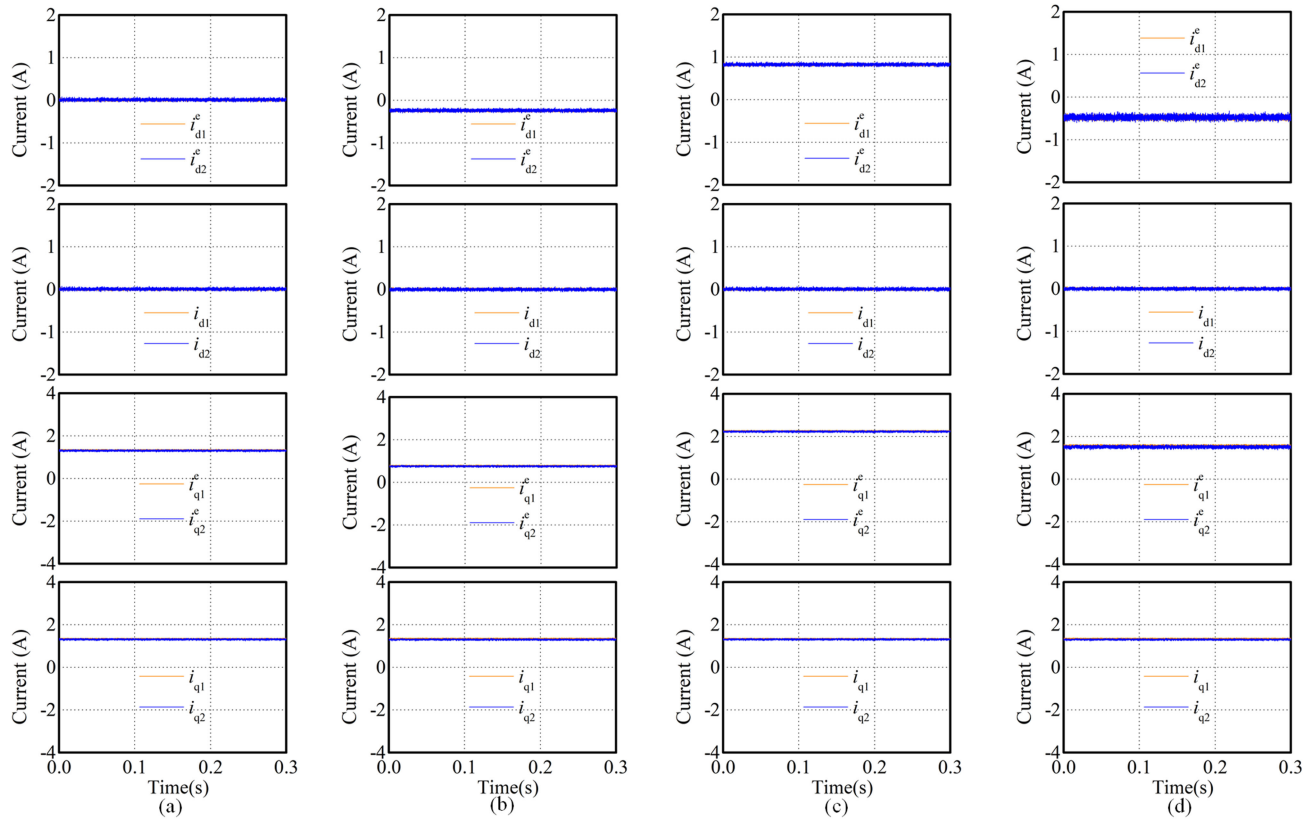

Fig. 8. Simulation results of C-FTC considering same parameter variations under (a) situation-1, (b) situation-2, (c) situation-3, and (d) situation-4.

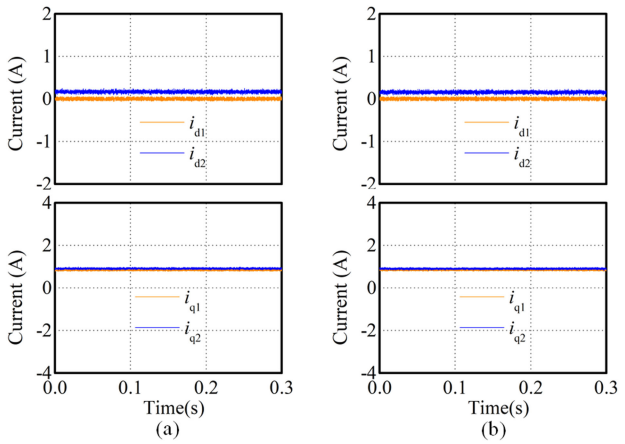

Fig. 9. Simulation results of C-FTC considering different parameter variations under (a) situation-3 and (b) situation-4.

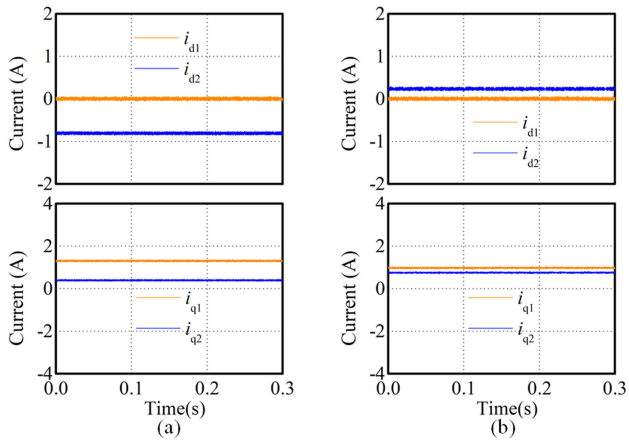

Fig. 10. Simulation results of I-FTC considering different parameter variations under (a) situation-3 and (b) situation-4.

variations in this simulation. It should be emphasized here that the difference of the parameter variations for two movers are usually not so significant in real subway applications. This setting with large differences of parameter variations is just to emphasize the comparison between C-FTC and I-FTC. The simulation results are illustrated in Figs. 9 and 10, where the performances of both C-FTC and I-FTC are affected. Comparing Fig. 9 with Fig. 10, however, it can be found that the differences of actual synchronous currents between two movers are significantly reduced by using C-FTC. Therefore, the performances of C-FTC are better than those of I-FTC if both movers have different parameter variations.

C. *Simulation 3: Affections of Nonlinear Effects*

In this simulation, only the nonlinear effects are considered while the parameter variations are neglected. The dead-time is

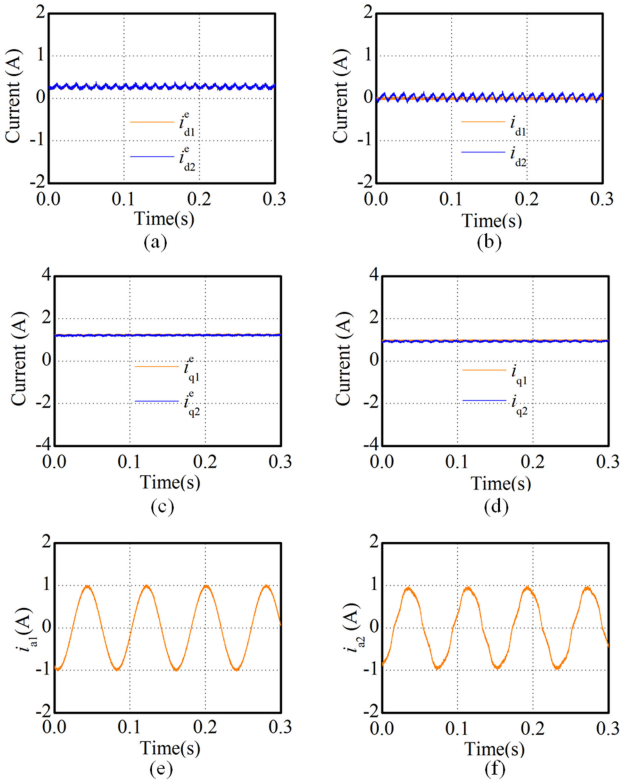

Fig. 11. Simulation results of C-FTC considering nonlinear effects. (a) Estimated d-axis currents. (b) Actual d-axis currents. (c) Estimated q-axis currents. (d) Actual q-axis currents. (e) Phase currents of mover 1. (f) Phase currents of mover 2.

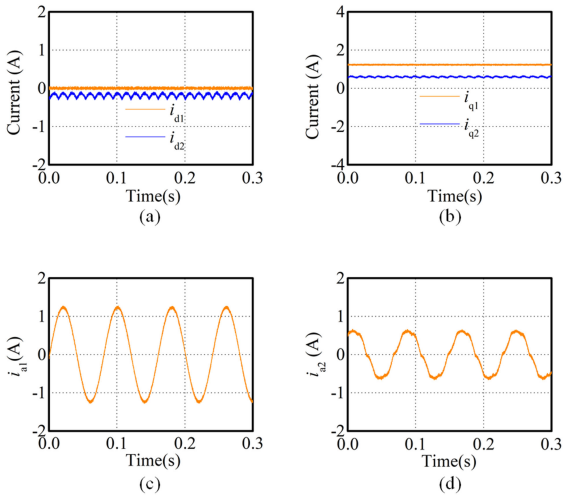

Fig. 12. Simulation results of I-FTC considering nonlinear effects. (a) Actual d-axis currents. (b) Actual q-axis currents. (c) Phase currents of mover 1. (d) Phase currents of mover 2.

set as 2 μs, and the voltage drop of power devices is set as 0.7 V. The simulation results using C-FTC and I-FTC are, respectively, illustrated in Figs. 11 and 12. As shown in Figs. 11 and 12, six harmonic components appear in the estimated currents of both movers and the actual currents of mover 2, which are resulted by the nonlinear effects of VSIs. The explanations about the six harmonic components can refer to [29]. Static current errors

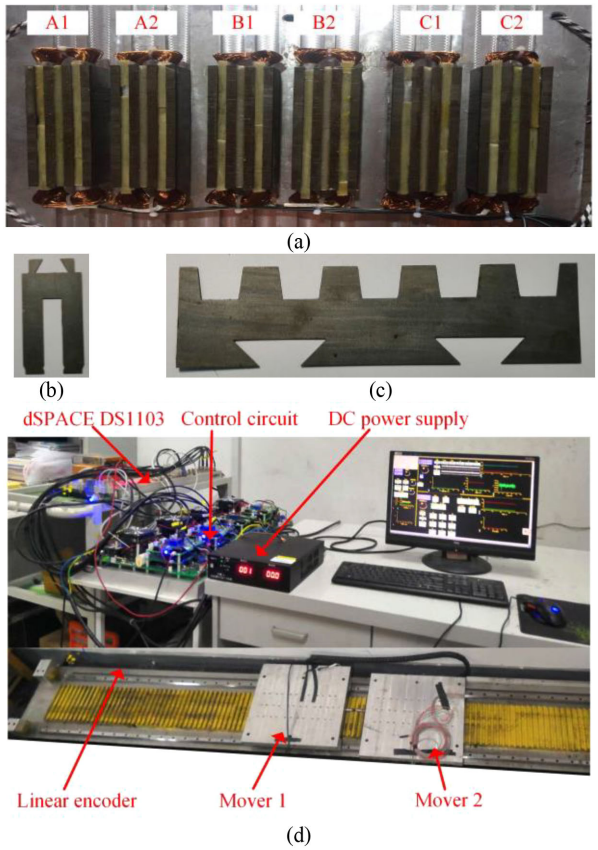

Fig. 13. Experiment platform. (a) Bottom view of mover. (b) Stator teeth. (c) Stator (rail) teeth. (d) Entire view.

appear in Fig. 12 while this phenomenon does not occur in Fig. 11. The reasons can be found in the Section IV-D.

VI. Experimental Validation

To verify the effectiveness of C-FTC, two same movers are manufactured and an experiment platform is developed, as shown in Fig. 13. The two movers with a linear encoder are connected together and their parameters are given in Table I. The control program is implemented in a dSPACE DS1103 controller. The inputs for the dSPACE DS1103 controller are the sensed phase currents and dc-link voltage, and the feedback signal of the linear encoder. It should be emphasized that the sensed and estimated phase currents are respectively used in HCCs of movers 1 and 2. The phase currents of mover 2 are just sensed as a reference but not used. The switch-states for the VSIs are generated by the dSPACE DS1103 controller. A personal computer is employed for editing the control program and commanding the dSPACE DS1103 controller. It should be emphasized that the d- and q-axis currents cannot be measured directly, and they are calculated from the measured phase currents according to Park transformation $\boldsymbol{P}(\theta_{e1})$ (10) in this section.

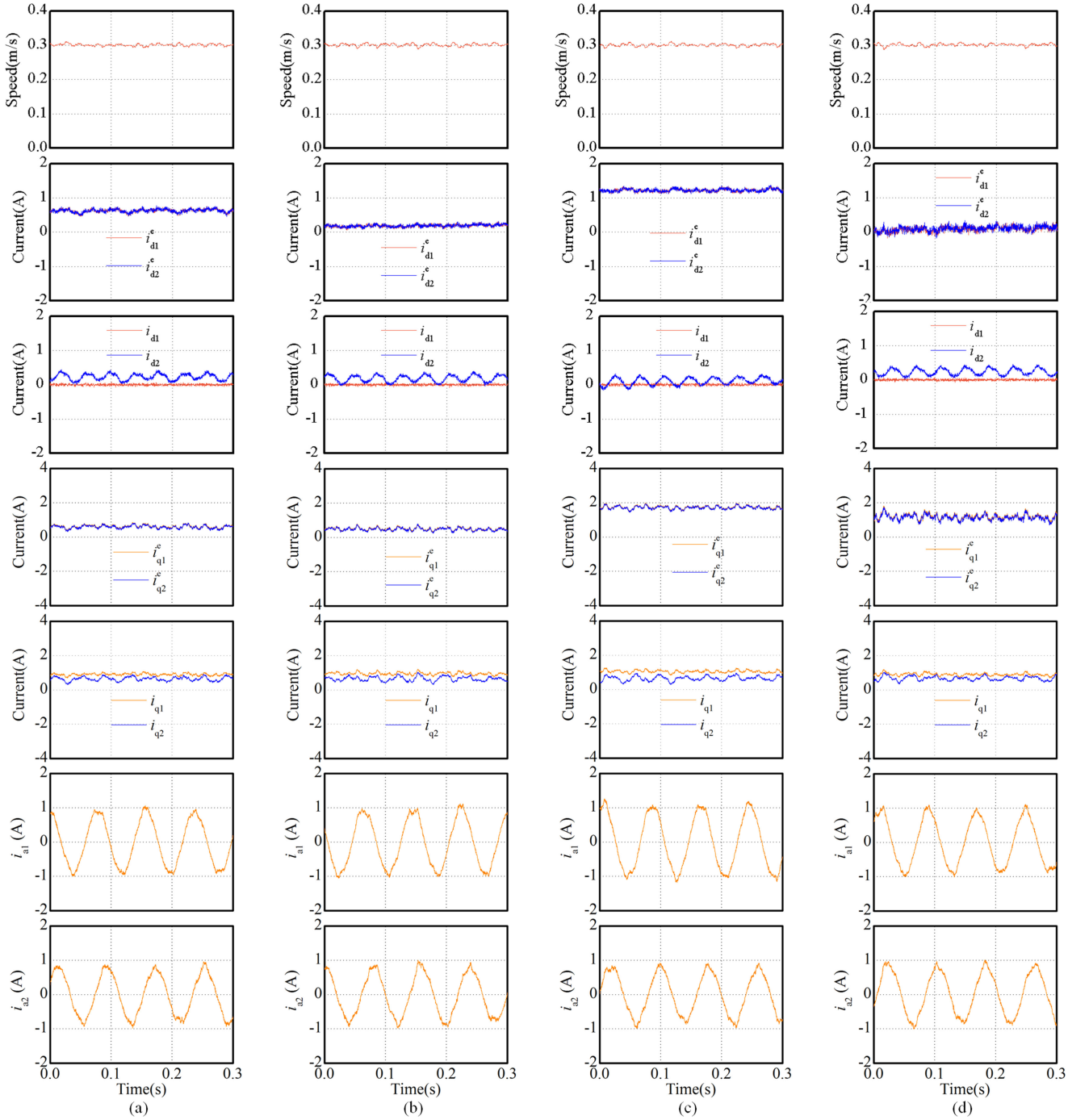

Fig. 14. Experimental results of steady-state operation using C-FTC under (a) situation-1, (b) situation-2, (c) situation-3, and (d) situation-4.

A. Experiment 1: Steady-State Performances of C-FTC

This experiment is to test steady-state performances of C-FTC. In this experiment, the speed reference is also set as 0.3 m/s. The experimental results under four situations as given in Table II are illustrated in Fig. 14. As shown in Fig. 14, the estimated synchronous currents (i^e_{d1},i^e_{q1}) are well tracked by (i^e_{d2},i^e_{q2}). However, the static errors between (i_{d1}, i_{q1}) and (i_{d2}, i_{q2}) appear, and the second harmonic components are significant in the actual synchronous currents (i_{d2}, i_{q2}). As analyzed in Section IV, the static errors of synchronous currents can be caused by different parameter variations or different nonlinear effects. Because the VSIs are mature commercial productions, the differences of nonlinear effects between two VSIs can be neglected. However, these two movers are manufactured in the lab, and their parameter consistency is not so good. As a result, the static current errors appear. Especially, L_{s2} contains significant second harmonic component, which results in the appearance of the second harmonic components in (i_{d2}, i_{q2}). However, it still can be found that the static current errors and

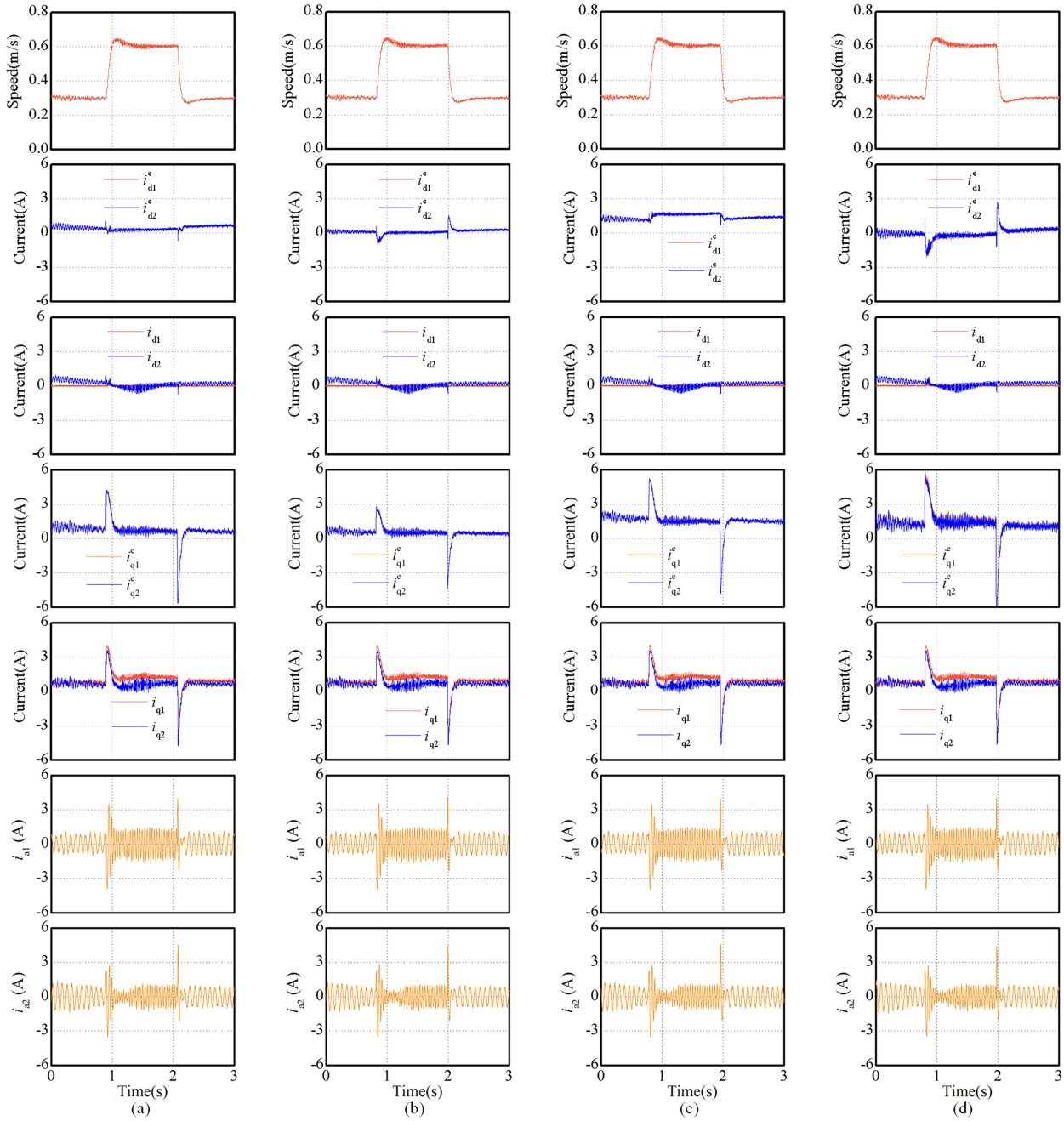

Fig. 15. Experimental results of speed response using C-FTC under (a) situation-1, (b) situation-2, (c) situation-3, and (d) situation-4.

the second harmonic components remain nearly unchanged in four different situations. In other words, the performances of C-FTC are not affected by same parameter variations. It should be emphasized that the differences of actual parameters between two movers can be quite small if they are manufactured in a mature commercial production line.

B. Experiment 2: Speed Response of C-FTC

In this experiment, the speed is increased from 0.3 to 0.6 m/s, and then decreased to 0.3 m/s. In order to verify the robustness of the proposed C-FTC, this speed response procedure is carried out in four different situations (situation-1–situation-4) to consider the parameter variations. The experimental results are illustrated in Fig. 15. In the speed response procedure, it can be found in Fig. 15 that the estimated synchronous currents (i^e_{d1}, i^e_{d2}, i^e_{q1}, i^e_{q2}) are significantly affected by the parameter variations while the differences between (i_{d1},i_{q1}) and (i_{d2}, i_{q2}) are nearly not affected by the same parameter variations. Hence, the performances of C-FTC are not affected during the speed response if both movers have same parameter variations.

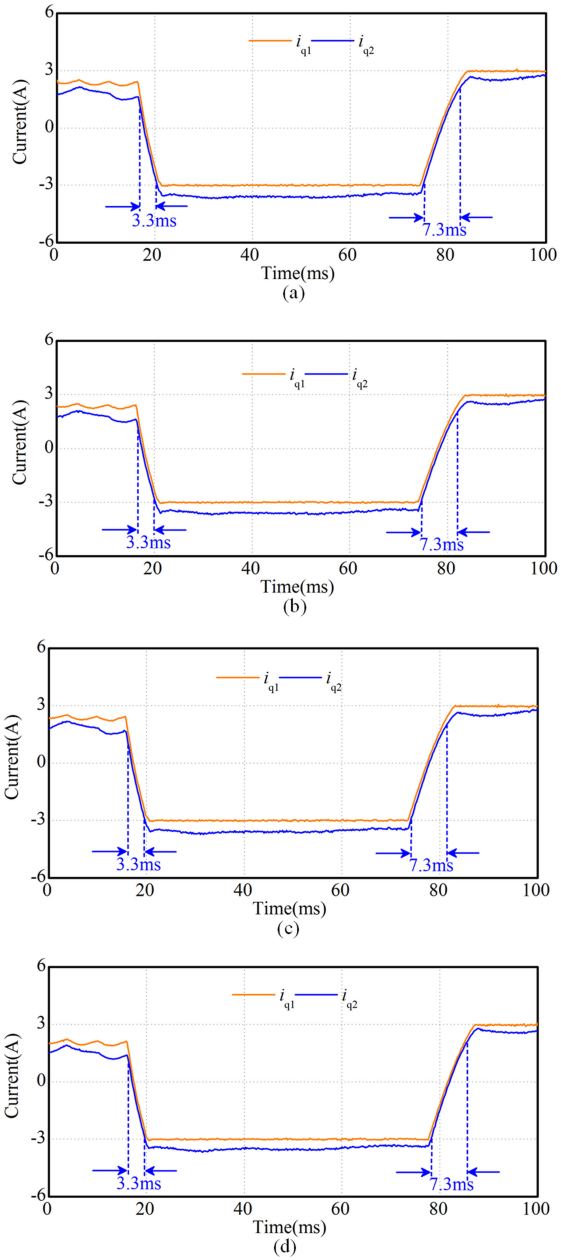

Fig. 16. Experimental results of current response performances using C-FTC under (a) situation-1, (b) situation-2, (c) situation-3, and (d) situation-4.

C. Experiment 3: Current Response of C-FTC

This experiment is to test the current response of C-FTC. In this experiment, the q-axis current of mover 1 is commanded to decrease from 3 to -3 A, and then return to 3 A. The experimental results under four situations are illustrated in Fig. 16. For mover 2, the falling time is measured from 1 to -3 A while the rising time is measured from –3 to 2 A, which are curved in Fig. 16. No matter in which situation, as shown in Fig. 16, the falling and rising times are 3.3 and 7.3 ms, respectively. Obviously, the current response ability of C-FTC is not affected by the parameter variations. It means the thrust response in post-fault operation can be as fast as that in normal operation for the traction system of subway applications, which is especially important for the safe operation in regenerative braking procedure.

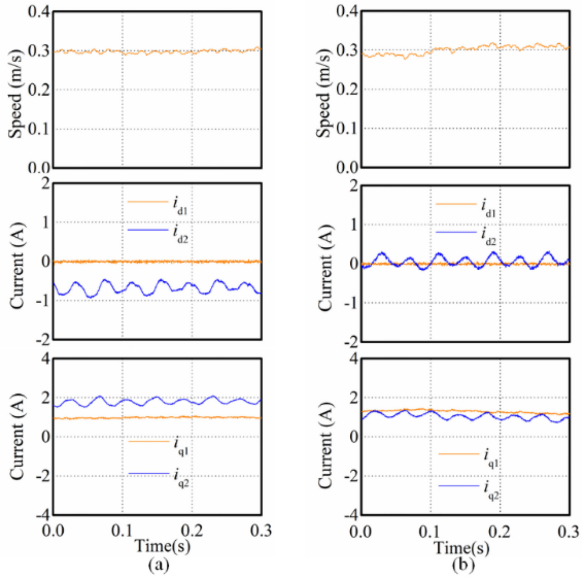

Fig. 17. Experimental results of steady-state operation under situation-1 using (a) I-FTC and (b) C-FTC.

D. Experiment 4: Comparison of I-FTC and C-FTC

In this experiment, the experimental parameters are set as situation-1. The experimental results using I-FTC and C-FTC are illustrated in Fig. 17. Comparing with I-FTC shown in Fig. 17(a), the differences between (i_{d1}, i_{q1}) and (i_{d2}, i_{q2}) have been significantly reduced by using C-FTC, which have been verified in Fig. 17(b). The reason is that the parameter variations and the nonlinear effects of mover 2 drive system have been mostly compensated by the parameter variations and the nonlinear effects of mover 1 drive system using C-FTC. However, no compensation for the parameter variations and the nonlinear effects of mover 2 drive system can be found since both movers are independent by using I-FTC.

VII. Conclusion

In this article, a C-FTC scheme without current sensor is proposed for the PPMLM traction system in subway applications, which takes full advantage of the multimotor feature. In the proposed C-FTC, a healthy mover is determined as the reference mover, and the faulty mover is coupled with the reference mover. The estimated synchronous currents of the reference mover are treated as the reference synchronous currents of the faulty mover, which are tracked by the estimated synchronous currents of the faulty mover. Comparing with the conventional CSC, the performances of C-FTC have been significantly improved by compensating the parameter variations and the nonlinear effects of the faulty mover drive system with those of a healthy mover drive system. The effectiveness and robustness of the proposed C-FTC are verified by simulation and experimental results. Comparing with the normal operation, the performances

of the PPMLM are degraded a bit in the fault-tolerant operation. Therefore, each mover is equipped with two current sensors in actual subway applications since the normal operation is preferable, and the proposed C-FTC is only a fault-tolerant solution coping with current sensor faults. In the future, the proposed C-FTC will be applied in a local subway line as soon as possible.

REFERENCES

[1] J. Q. Li, W. L. Li, G. Q. Deng, and Z. Ming, "Continuous-behavior and discrete-time combined control for linear induction motor-based urban rail transit," *IEEE Trans. Magn.*, vol. 52, no. 7, Jul. 2016, Art. no. 8500104.

[2] W. Xu, X. Xiao, G. Du, D. Hu, and J. Zou, "Comprehensive efficiency optimization of linear induction motors for urban transit," *IEEE Trans. Veh. Technol.*, vol. 69, no. 1, pp. 131–139, Jan. 2020.

[3] G. Lv, T. Zhou, D. Zeng, and Z. Liu, "Influence of secondary constructions on transverse forces of linear induction motors in curve rails for urban rail transit," *IEEE Trans. Ind. Electron.*, vol. 66, no. 6, pp. 4231–4239, Jun. 2019.

[4] L. Yan, "The linear motor powered transportation development and application in China," *Proc. IEEE*, vol. 97, no. 11, pp. 1872–1880, Nov. 2009.

[5] R. Cao, E. Su, M. Lu, J. Si, and K. Wang, "Investigation of linear synchronous reluctance motor for urban rail transit," *IET Elect. Power Appl.*, vol. 14, no. 1, pp. 41–51, Jan. 2020.

[6] R. Hellinger and P. Mnich, "Linear motor-powered transportation: History, present status, and future outlook," *Proc. IEEE*, vol. 97, no. 11, pp. 1892–1900, Nov. 2009.

[7] G. Lv, T. Zhou, D. Zeng, and Z. Liu, "Design of ladder-slit secondaries and performance improvement of linear induction motors for urban rail transit," *IEEE Trans. Ind. Electron.*, vol. 65, no. 2, pp. 1187–1195, Feb. 2018.

[8] W. Wang, W. Tian, Z. Wang, W. Hua, and M. Cheng, "A fault diagnosis method for current sensors of primary permanent-magnet linear motor drives," *IEEE Trans. Power Electron.*, to be published, doi: 10.1109/TPEL.2020.3011125.

[9] Z. Zhang, H. Zhou, J. Duan, and B. Kou, "Research on permanent magnet linear synchronous motors with ring windings for electromagnetic launch system," *IEEE Trans. Plasma Sci.*, vol. 45, no. 7, pp. 1161–1167, Jul. 2017.

[10] R. Cao, M. Lu, N. Jiang and M. Cheng, "Comparison between linear induction motor and linear flux-switching permanent-magnet motor for railway transportation," *IEEE Trans. Ind. Electron.*, vol. 66, no. 12, pp. 9394–9405, Dec. 2019.

[11] Q. Lu, Y. Yao, J. Shi, Y. Shen, X. Huang, and Y. Fang, "Design and performance investigation of novel linear switched flux PM machines," *IEEE Trans. Ind. Appl.*, vol. 53, no. 5, pp. 4590–4602, Sep./Oct. 2017.

[12] M. Zhao *et al.*, "Development and analysis of novel flux switching transverse flux permanent magnet linear machine," *IEEE Trans. Ind. Electron.*, vol. 66, no. 6, pp. 4923–4933, Jun. 2019.

[13] W. Zhao, B. Wu, Q. Chen, and J. Zhu, "Fault-tolerant direct thrust force control for a dual inverter fed open-end winding linear vernier permanent-magnet motor using improved SVPWM," *IEEE Trans. Ind. Electron.*, vol. 65, no. 9, pp. 7458–7467, Sep. 2018.

[14] W. Wang, Z. Lu, W. Hua, Z. Wang, and M. Cheng, "Dual-level located feedforward control for five-leg two-mover permanent-magnet linear motor traction systems," *IEEE Trans. Power Electron.*, vol. 35, no. 12, pp. 13673–13686, Dec. 2020.

[15] C. Wu, C. Guo, Z. Xie, F. Ni, and H. Liu, "A signal-based fault detection and tolerance control method of current sensor for PMSM drive," *IEEE Trans. Ind. Electron.*, vol. 65, no. 12, pp. 9646–9657, Dec. 2018.

[16] I. Jlassi, J. O. Estima, S. K. El Khil, N. M. Bellaaj, and A. J. M. Cardoso, "A robust observer-based method for IGBTs and current sensors fault diagnosis in voltage-source inverters of PMSM drives," *IEEE Trans. Ind. Appl.*, vol. 53, no. 3, pp. 2894–2905, May/Jun. 2017.

[17] S. C. Chang and S. N. Yeh, "Current sensorless field-oriented control of induction motors," *IEE Proc. Elect. Power Appl.*, vol. 143, no. 6, pp. 492–500, Nov. 1996.

[18] S. Morimoto, M. Sanada, and Y. Takeda, "High-performance current-sensorless drive for PMSM and SynRM with only low-resolution position sensor," *IEEE Trans. Ind. Appl.*, vol. 39, no. 3, pp. 792–801, May/Jun. 2003.

[19] M. Khayamy and H. Chaoui, "Current sensorless MTPA operation of interior PMSM Drives for vehicular applications," *IEEE Trans. Veh. Technol.*, vol. 67, no. 8, pp. 6872–6881, Aug. 2018.

[20] K. Xiahou, X. Lin, Y. Liu, and Q. H. Wu, "Robust rotor-current sensorless control of doubly fed induction generators," *IEEE Trans. Energy Convers.*, vol. 33, no. 2, pp. 897–899, Jun. 2018.

[21] C. Chakraborty and V. Verma, "Speed and current sensor fault detection and isolation technique for induction motor drive using axes transformation," *IEEE Trans. Ind. Electron.*, vol. 62, no. 3, pp. 1943–1954, Mar. 2015.

[22] W. Wang, Y. Feng, Y. Shi, M. Cheng, W. Hua, and Z. Wang, "Fault-tolerant control of primary permanent-magnet linear motors with single phase current sensor for subway applications," *IEEE Trans. Power Electron.*, vol. 34, no. 11, pp. 10546–10556, Nov. 2019.

[23] M. Manohar and S. Das, "Current sensor fault-tolerant control for direct torque control of induction motor drive using flux-linkage observer," *IEEE Trans. Ind. Inf.*, vol. 13, no. 6, pp. 2824–2833, Dec. 2017.

[24] Y. Yu, Y. Zhao, B. Wang, X. Huang, and D. Xu, "Current sensor fault diagnosis and tolerant control for VSI-based induction motor drives," *IEEE Trans. Power Electron.*, vol. 33, no. 5, pp. 4238–4248, May 2018.

[25] Y. Xu, H. Yan, J. Zou, B. Wang, and Y. Li, "Zero voltage vector sampling method for PMSM three-phase current reconstruction using single current sensor," *IEEE Trans. Power Electron.*, vol. 32, no. 5, pp. 3797–3807, May 2017.

[26] J. Lu, Y. Hu, and J. Liu, "Analysis and compensation of sampling errors in TPFS IPMSM drives with single current sensor," *IEEE Trans. Ind. Electron.*, vol. 66, no. 5, pp. 3852–3855, May 2019.

[27] F. Blaabjerg, J. K. Pedersen, U. Jaeger, and P. Thoegersen, "Single current sensor technique in the DC link of three-phase PWM-VS inverters: A review and a novel solution," *IEEE Trans. Ind. Appl.*, vol. 33, no. 5, pp. 1241–1253, Sep./Oct. 1997.

[28] W. Wang, Y. Feng, Y. Shi, M. Cheng, W. Hua, and Z. Wang, "Direct thrust force control of primary permanent-magnet linear motors with single DC-link current sensor for subway applications," *IEEE Trans. Power Electron.*, vol. 35, no. 2, pp. 1365–1376, Feb. 2020.

[29] S.-H. Hwang and J.-M. Kim, "Dead-time compensation method for voltage-fed PWM inverter," *IEEE Trans. Energy Convers.*, vol. 25, no. 1, pp. 1–10, Mar. 2010.

Wei Wang (Senior Member, IEEE) was born in Jiangsu, China. He received the B.Sc. degree from the Nanjing University of Science and Technology, Nanjing, China, in 2008, and the Ph.D. degree from Southeast University, Nanjing, China, in 2014, respectively, all in electrical engineering.

Since 2014, he has been with Southeast University, Nanjing, China, where he is currently an Associate Professor with the School of Electrical Engineering. From 2011 to 2012, he received the Scholarship from China Scholarship Council and was a joint Ph.D student with University of Lille 1, Lille, France. He is the author or co-author of more than 30 technical papers. His research interests include motor drives and electrified transport.

Zhixiang Lu was born in Jiangsu Province, China. He received the B.Sc. degree in electrical engineering from the Nanjing University of Science and Technology, Nanjing, China, in 2018. He is currently working toward the M.Sc. degree in electrical engineering with Southeast University, Nanjing.

His current research interests include electrical drives and model predictive control.

Yanan Feng was born in Anhui, China. He received the B.Sc. degree from Anhui University of Technology, Maanshan, China, in 2016, and the M. Sc. degree from Southeast University, Nanjing, China, in 2019, respectively, all in electrical engineering.

Since 2020, he has been with Huzhou University, Huzhou, China. His current research interests include electromagnetic analysis and control of permanent magnet linear motor and traction system of rail transit.

Weijie Tian was born in Jiangsu Province, China. He received the B.Sc. degree in electrical engineering from Shenyang University of Technology, Shenyang, China, in 2018. He is currently working toward the M.Sc. degree in electrical engineering with Southeast University, Nanjing, China.

His current research interests include fault diagnosis and control of electrical machine drive systems.

Wei Hua (Senior Member, IEEE) was born in Taizhou, China, in 1978. He received the B.Sc. and Ph.D. degrees in electrical engineering from Southeast University, Nanjing, China, in 2001 and 2007, respectively.

Since 2007, he has been with Southeast University, where he is currently a Professor with the School of Electrical Engineering. He is the author or co-author of more than 100 technical papers and is the holder of 44 patents in his areas of interest. His research interests include the design, analysis, and control of electrical machines.

Zheng Wang (Senior Member, IEEE) received the B.Eng. and M.Eng. degrees from Southeast University, Nanjing, China, in 2000 and 2003, respectively, and the Ph.D. degree from The University of Hong Kong, Hong Kong, in 2008.

From 2008 to 2009, he was a Postdoctoral Fellow with Ryerson University, Toronto, ON, Canada. He is currently a Full Professor with the School of Electrical Engineering, Southeast University, China. He has authored or coauthored more than 80 internationally refereed papers and four books in these areas. His research interests include electric drives, power electronics, and distributed generation.

Dr. Wang received several academic awards including IEEE PES Chapter Outstanding Engineer Award, Best Paper Award of International Conference on Electrical Machines and Systems, Best Session Paper Award of IEEE Annual Meeting of Industrial Electronics, and Nanjing Outstanding Paper Award of Natural Science.

Ming Cheng (Fellow, IEEE) received the B.Sc. and M.Sc. degrees from the Department of Electrical Engineering, Southeast University, Nanjing, China, in 1982 and 1987, respectively, and the Ph.D. degree from the Department of Electrical and Electronic Engineering, University of Hong Kong, Hong Kong, in 2001.

Since 1987, he has been with Southeast University, where he is currently a Distinguished Professor with the School of Electrical Engineering and the Director of the Research Center for Wind Power Generation. From January to April 2011, he was a Visiting Professor with the Wisconsin Electric Machine and Power Electronics Consortium, University of Wisconsin Madison, WI, USA. He has authored or coauthored more than 300 technical papers and four books, and is the holder of 70 patents in these areas. His research interests include electrical machines, motor drives for EV, and renewable energy generation.

Dr. Cheng is a fellow of the Institution of Engineering and Technology. He was the Chair and Organizing Committee Member for many international conferences. He is a Distinguished Lecturer of the IEEE Industry Applications Society from 2015 to 2016.